Fracture-directed Waterjet Needle Steering: Design, Modeling, and Path Planning

Mahdieh Babaiasl[1], Fan Yang[2], Stefano Boccelli[3], and John P. Swensen[4]

***Abstract*— Steerable needle technology has the promise of improving outcomes by enhancing the accuracy of different therapies and biopsies, as they can be steered to a target location around obstacles. Achieving small radius of curvature and being able to control both radius of curvature and tip travel are of paramount importance in steerable needles to accomplish the increase in efficacy of the medical procedures. In this paper, we present a new class of the steerable needles, which we call waterjet-directed steerable needles, where the underlying principle is to first control the direction of tissue fracture with waterjet, after which the needle will follow during subsequent insertion. In this paper, the direction of the tissue fracture is controlled by an angled waterjet nozzle and control of the water velocity, and then the flexible Nitinol needle follows. It is shown that by changing the velocity of waterjet and thus depth of cut, radius of curvature can be controlled. A discrete-step kinematic model is used to model the motion of the waterjet steerable needle. This model consist of two parts: (1) the mechanics-based model predicts the cut-depth of waterjet in soft tissue based on soft tissue properties, waterjet diameter, and water exit velocity, and (2) a discrete-step kinematic unicycle model of the steerable needle travel. Path planning is accomplished through a genetic algorithm, and the efficacy of waterjet steerable needle is tested for different paths. The key finding of the paper is that the radius of curvature of the waterjet steerable needle can be controlled by a fixed waterjet tip angle and varying water exit velocity to control the depth of cut.**

I. INTRODUCTION

Recent developments in steerable needle technology have shown clinical potential to improve the outcomes of different procedures such as lung access [1], target access in the breast [2], and improving brachytherapy with steerable needles [3]. The current needle steering approaches consist of bevel-tipped steering, pre-bend steering, duty-cycle steering, external lateral manipulation [4], and active cannulae [5], [6]. Most of these approaches rely on creating an asymmetric force at the tip of the needle to guide the steering [7], [8], [9]. Among these methods, pre-bend steerable needles achieved the best radius of curvature to date, however, they can lead to undesirable deformations and damage to the tissue due to relying on duty cycling to control the curvature. A complete discussion on the current limitations of the steerable needles is provided in [10]. Other approaches for needle steering include a loop-shaped flexible mechanism [11], notched steerable needles [12], and magnetic steering [13]. Current research mostly focuses on improving control mechanisms of the steerable needles as well as transferring these needles from laboratory to clinical settings [14], [15], [16], [17]. Considering the limitations of current steerable needles specifically effect of torsional friction while duty cycling [18], proposing new ways to control the curvature of the steerable needles seems to be necessary.

This paper presents a new strategy for achieving significantly greater control over the direction of the tissue fracture, which we call waterjet-directed steerable needles, and is part of the larger class of fracture-directed steerable needles [19]. In fracture-directed steerable needles, the underlying principle is that the direction of the tissue fracture is accurately controlled, after which subsequent insertion of the needle will follow the fracture direction. In the present work, the fracture direction is achieved through the direction of the waterjet nozzle relative to the needle tip and the velocity of the water exiting the nozzle to control the depth of the tissue fracture.

This paper explores the effect of waterjet velocity, and thus length of cut channel on achievable radius of curvature of the needle in two tissue stiffnesses. A kinematic model relating the depth of cut and the base rotation to the motion of the needle is presented. The main advantage of the proposed method is being able to control the curvature of the needle by simply controlling the velocity of the waterjet (and thus cut-depth), with future work on both nozzle angle and waterjet velocity.

Fig. 1 shows the principle of the fracture-directed waterjet steerable needles, where the waterjet first cuts a small angled path in tissue (depth of cut), and then the flexible Nitinol tube follows the path. This process continues until the waterjet needle can be steered around obstacles to reach to a desired target.

II. MATERIALS AND METHODS

In this section, the materials and methodology used for soft tissue preparation, the tests to characterize tissue properties, the experimental setup used for experiments, the curvature measurements of the waterjet steerable needle, the modeling of the needle motions, and the path planning algorithm are described.

[1]Mahdieh Babaiasl is a graduate research assistant with the School of Mechanical and Materials Engineering, Washington State University, Pullman, Washington, USA. mahdieh.babaiasl@wsu.edu

[2]Fan Yang is a graduate research assistant with the School of Mechanical and Materials Engineering, Washington State University, Pullman, Washington, USA. fan.yang6@wsu.edu

[3]Stefano Boccelli is a graduate research assistant with the Department of Aerospace Science and Technology, Politecnico di Milano, Milan, Italy. stefano.boccelli@polimi.it

[4]John P. Swensen is an assistant professor with the School of Mechanical and Materials Engineering, Washington State University, Pullman, Washington, USA. john.swensen@wsu.edu

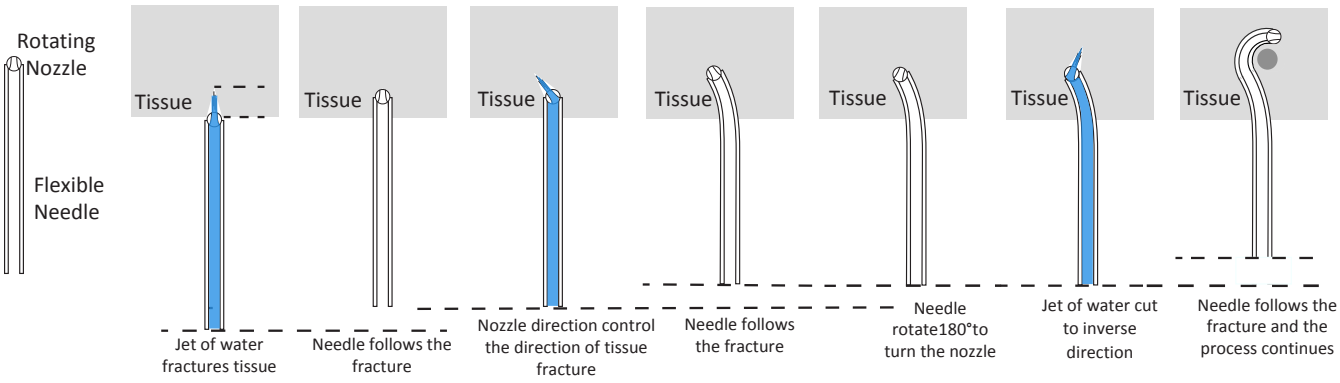

Fig. 1. Principle of Fracture-directed Waterjet Steerable Needles. First, Waterjet from an angled nozzle cuts a small path in tissue, and then the flexible needle follows the fractured path. This process continues until the needle goes around obstacles, and reaches to a target location.

A. Tissue Simulant Preparation and Mechanical Testing

Because of the difficulties associated with using real biological tissues (a complete list of difficulties are discussed in our other publications. The interested reader is referred to [20] for more information.), we have used Poly (styrene-b-ethylene-co-butylene-b-styrene) triblock copolymer (SEBS) by Kraton Polymers LLC (G1650, Houston, TX, USA) as the main material for our tissue-mimicking simulants. The solvent used for SEBS is light mineral oil, which makes it a more environmentally stable substitute for water-based hydrogels [21], [19]. To make the tissue simulants, SEBS material and mineral oil are weighed out to produce mixtures with 10, and 15 vol% SEBS. The mixture is then put in the oven at $150°C$ for about 2 to 6 hours based on the percentage of SEBS, and it was mixed from time to time to get a homogeneous solution without any undissolved powder. After this time, the solution is degassed in a vacuum chamber to eliminate any air bubbles trapped in the solution. The solution is then poured into molds of $100 \times 100 \times 30$ mm, and then let cool down to room temperature and solidify before releasing from the molds. One of the most attractive features of SEBS is the ability to accurately control the elastic properties of the materials through control of the volume fractions of SEBS powder and mineral oil solvent [22].

Low strain rate static compression, high strain rate split-Hopkinson-pressure-bar (SHPB), and fracture toughness tests were conducted on SEBS soft tissue simulants to characterize the tissue phantoms. Uniaxial compressive strains of up to 0.7 is applied. The high strain rate tests are conducted to have the tissue properties at strain rates associated with waterjet velocities. A first-order Ogden model was used to find the shear modulus and strain hardening factor of the soft tissues at different waterjet velocities. These results are used to predict the depth of cut of waterjet in soft tissue based on tissue, and waterjet properties.

B. Experimental Setup

The experimental setup is depicted in Fig. 2. A high pressure pump (PR-class Dual Piston, PR100PFT3D, Scientific Systems Inc., State College, PA, USA) provides a computer-controlled volumetric flow rate (up to $100\frac{mL}{min}$). When the water velocity exceeds the threshold necessary to fracture the tissue, a channel will be cut at 30° relative to tangent to the needle tip, due to the nozzle design. The desired depth of cut is controlled by the time and duration of the waterjet at a specific water velocity. After a channel is cut by waterjet, the pump is turned off and the needle is advanced to follow the cut channel with a velocity of insertion of 1 $\frac{mm}{s}$. This insertion velocity is known to be relevant to insertions in real medical applications [23]. Through varying the waterjet velocity to control the cut-depth, subsequent insertion of the needle to follow the fractions, and reorientation of the needle tip through whole-needle rotation, the waterjet needle can be steered in the soft tissue. A 3D-printed custom-designed box along, with suction canister and a vacuum pump, are used to collect the water that leaks back out along the shaft of the needle during experiments. Future design will include a dual-lumen needle for suction of the introduced fluid, if necessary.

The insertion unit consists of two components, a 85mm long nickel-titanium tube (GoodFellow Corporation, Coraopolis, PA) and a 6.85mm long 3D-printed polycaprolactone (PCL) nozzle. The nickel-titanium tube has 0.33mm outer diameter with 0.24mm inner diameter, and the PCL nozzle has 1.6mm outer diameter with 0.33mm inner diameter at the base and 0.24mm diameter at the tip. The PCL nozzle was 3D-printed by FDM printer then attached to the nickel-titanium tube using cyanocrylate glue.

C. Curvature measurement of waterjet steerable needle

In order to measure the radius of curvature of the needle path, 10%, and 15% SEBS in mineral oil soft tissue simulants are used. Two velocities of water are tested for each soft tissue simulant in order to study the effect of the waterjet velocity, and thus depth-of-cut, on the radius of curvature. Three tests are done for each velocity of the waterjet and the average radii for the tests are presented. The radius of curvature is measured by fitting a circle to the path of the needle using image processing software. The curvature (κ) of the needle can simply be calculated by inverting the radius of curvature (r):

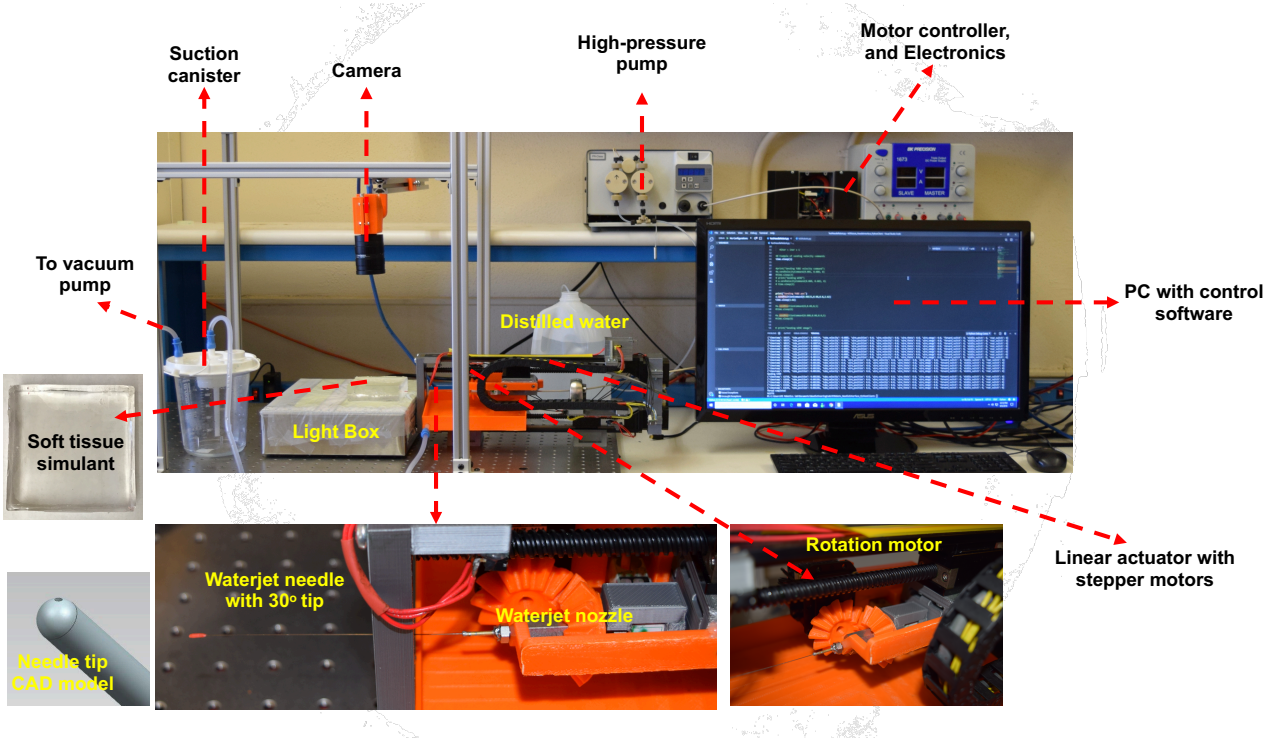

Fig. 2. Experimental setup for waterjet needle steering. First, high-pressure pump is set to the desired flow rate based on the desired depth-of-cut, and then waterjet cuts a channel in tissue at 30°, the pump is turned off and the needle follows the channel with the velocity of insertion of 1 $\frac{mm}{s}$. This process continues until the needle is steered in the tissue.

$$\kappa = \frac{1}{r} \tag{1}$$

D. Model of waterjet needle

In this subsection, the model of the needle motion is described that consist of a mechanics-based model for the prediction of the depth of cut of waterjet in soft tissue and a kinematics model to describe the needle path using this computed depth of cut.

1) Depth-Of-Cut model: We have developed a mechanics-based model for depth of cut of waterjet in soft tissue that predicts the depth of cut based on tissue mechanical properties (constitutive response, and fracture toughness), as well as waterjet properties (diameter and velocity). The cut-depth of waterjet in soft tissue can be expressed by the following ordinary differential equation, where A_{surf} and A_{out} are functions of h. This equation can be readily integrated using standard methods such as Runge-Kutta integrators:

$$\frac{\mathrm{d}h}{\mathrm{d}t} = \frac{1}{P_w}\frac{\rho Q^3}{\pi^3 R^6}\frac{A_{\text{inj}}A_{\text{surf}}}{(A_{\text{surf}}+A_{\text{out}})^2} \tag{2}$$

Here, h is the depth of cut, and P_w, ρ, Q, R, A_{inj}, A_{surf}, and A_{out} are penetration pressure of the waterjet (Pa), density of the water ($\frac{kg}{m^3}$), volumetric flow rate of the waterjet ($\frac{m^3}{s}$), needle inner radius (in our case: $2R = 0.24mm$), and injection, surface, and backflow areas (m^2), respectively. The penetration pressure of the waterjet in soft tissue can be expressed by the following equation:

$$P_w = \frac{4}{D(1-(\frac{d}{D})^2)}\{J_{IC}(\frac{d}{D}) + \frac{D}{4}\frac{2\mu}{\alpha^2}[\int_1^{\infty} f(\frac{d}{D},\gamma)d\gamma + 2(\frac{d}{D})^{2-\alpha} + (\frac{d}{D})^{2\alpha+2} - 3(\frac{d}{D})^2]\}, \tag{3}$$

in which, D, d, J_{IC}, α, μ, ρ, v, and T are waterjet diameter, steady-state diameter after waterjet removal, mode I fracture toughness, strain hardening factor, shear modulus, water density, waterjet velocity, and time, respectively. Function $f(\frac{d}{D},\gamma)$ can be expressed in the closed form as:

$$f(\frac{d}{D},\gamma) = (\frac{\gamma+(\frac{d}{D})^2-1}{\gamma})^{\frac{\alpha}{2}} + (\frac{\gamma}{\gamma+(\frac{d}{D})^2-1})^{-\frac{\alpha}{2}} - 2 \tag{4}$$

Both the function f and the parameter γ are sub-computations that facilitate the derivation and computations of the integral, and do not have any significant physical meaning.

2) Nonlinear kinematic model of the waterjet needle steering: The kinematic model of the waterjet needle steering presented in this paper is an adaptation of the unicycle model presented in [24], [25]. Fig. 3 depicts the nonlinear kinematic model of needle steering. In this case, $\delta\theta$, $\delta\ell$, and r are the incremental needle rotation angle, incremental insertion distance, and radius of curvature. $\delta\ell$ is equal to the the depth of cut (h) of the waterjet in each step and if the number of steps is n, then the whole insertion length is $\ell = \delta\ell \times n$. In order to change the direction of the needle to re-orient the x-y plane in any given step $\delta\theta$ should be applied to rotate

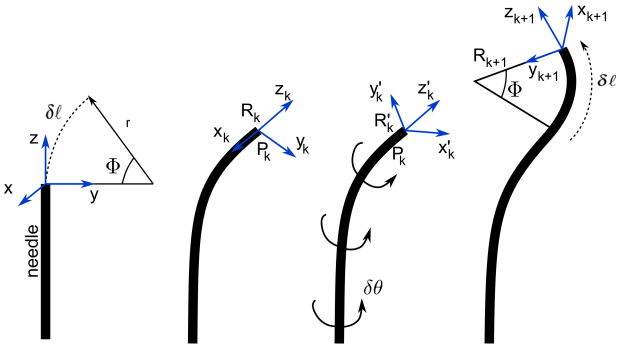

Fig. 3. The kinematic model of needle steering. The z-axis is assumed to be tangent to the needle at the tip, and the y-axis is towards the center of the curvature. The needle follows a path in y-z plane with radius r and arc length ℓ. The frame advances as the needle tip progresses during waterjet needle steering. $\delta\theta$, $\delta\ell$, and r are the incremental needle rotation angle, incremental insertion distance, and radius of curvature, respectively. Note that, in this paper $\delta\ell$ equals h (depth-of-cut).

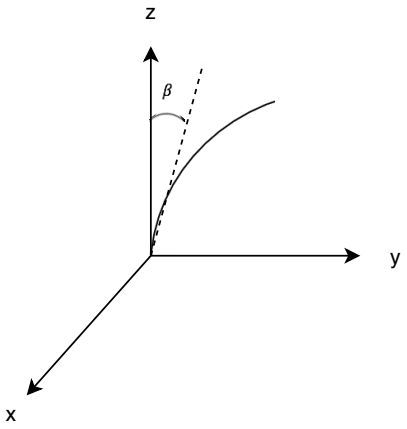

Fig. 4. Definition of β in (8). β is defined as the deflection of the needle around x-axis.

the needle at its base and thus reorient the nozzle at the tip. In this model, the pose of the needle is described by the pose of the needle tip frame with respect to a reference frame. The needle has a position of $\mathbf{p}_k$ and rotation $\mathbf{R}_k$ at time k. Rotation of $\delta\theta$ about the z-axis gives the rotated tip frame $\mathbf{R}'_k = \mathbf{R}_k\mathbf{R}_z(\delta\theta)$. The position of the needle tip after insertion of $\delta\ell$ can be calculated from the geometry of the circular path as:

$$\mathbf{p}^{k'}_{k+1} = \begin{bmatrix} 0 \\ r(1-cos(\Phi)) \\ rsin(\Phi) \end{bmatrix}, \tag{5}$$

where $\Phi = \frac{\delta\ell}{r}$. The position of the needle tip at time $k+1$, can be found by transforming this vector into the world frame:

$$\mathbf{p}_{k+1} = \mathbf{R}_k\mathbf{R}_z(\delta\theta)\mathbf{p}^{k'}_{k+1} + \mathbf{p}_k \tag{6}$$

Tip orientation at time $k+1$ can be calculated by:

$$\mathbf{R}_{k+1} = \mathbf{R}_k\mathbf{R}_z(\delta\theta)\mathbf{R}_x(-\Phi) \tag{7}$$

Note that:

$$\mathbf{R}_0 = \mathbf{R}_x(-\beta) = \begin{bmatrix} 1 & 0 & 0 \\ 0 & cos(\beta) & sin(\beta) \\ 0 & -sin(\beta) & cos(\beta) \end{bmatrix}, \tag{8}$$

Where $\mathbf{R}_0$ is the rotation matrix around x-axis by a deflection angle of $-\beta$. β is defined as shown in Fig. 4:

E. 2D path planning using a genetic algorithm

The optimal path planning is designed using a genetic algorithm (GA) in the environment map. The environment in the current study is a soft tissue. The tissue is discretized into parts divided into longitudinal and transverse directions. A value has been assigned to every point in this set of discrete parts, which is defined by a softness function. The softness function helps to penalize the desired distance from any obstacle. The softness value is minimal for normal points and is large for obstacles:

$$\text{softness}(y,z) = \begin{cases} 1 & \text{normal points} \\ 10^{10} & \text{obstacle points} \end{cases} \tag{9}$$

The genetic algorithm is used to make an optimized path. Every path can be constructed from some $\delta\ell$, $\delta\theta$, and r, which are the incremental path length (in our case depth of cut), incremental needle base rotation, and radius of curvature, respectively. r is a function of $\delta\ell$, and tissue type, and in this paper we measured r experimentally, so there are just two parameters that need to be optimized, that are $\delta\ell$, and $\delta\theta$. Therefore, a path can be displayed in the following form:

$$\begin{array}{cc} \delta\ell & \delta\theta \\ value_1 & value_1 \\ value_2 & value_2 \\ . & . \\ . & . \\ . & . \end{array} \Big| \downarrow \text{steps} \tag{10}$$

For the first step of the genetic algorithm (initial population), some paths are randomly created with constant step size and evaluated by the cost function explained below.

The cost function consists of 3 terms. The first term includes the length of the path, the second term is related to the softness value of the environment, and the third one is about the distance of the needle tip from the target point. As mentioned before, the tissue is discretized into some points in y, and z coordinates. Every point of these coordinates of tissue has a value. This value is minimal for normal points and a big amount (here 10^{10}) for obstacle points. Therefore, when a path crosses an obstacle, the cost function would be so large, and large amounts of the cost function cause the path to be excluded from optimization process in subsequent iterations. Also, because the distance of the target point is very important, this distance will be multiplied in a large number (here 10^{10}) to bring out the paths with large distances

of the target from the optimization process in subsequent iterations. The cost is defined as follows:

$$\text{cost} = c_1 + c_2 + c_3 \tag{11}$$

Where c_1, c_2, and c_3 are the costs related to the path, the environment, and the distance from the target:

$$c_1 = \sum_{i=1}^{n} \delta\ell_i \tag{12}$$

$$c_2 = \sum_{r=1}^{m} \text{softness}(y_r, z_r) \tag{13}$$

$$c_3 = 10^{10}\sqrt{(X-x_f)^2 + (Y-y_f)^2 + (Z-z_f)^2} \tag{14}$$

Where, n,and m are the number of steps of the needle following the cut path by waterjet, and the number of points (cells) that the paths cross them in the environment, respectively. $\begin{bmatrix} X & Y & Z \end{bmatrix}^T$, and $\begin{bmatrix} x_f & y_f & z_f \end{bmatrix}^T$ are the coordinates of the ending point of the path (needle tip), and the desired target point, respectively. The needle tip position can be obtained using kinematic model of the needle in (6), and (7). (y_r, z_r) are the cells' coordinates that the needle crosses them. These cells can be obtained using kinematic model of the needle.

The initial population is evaluated by cost function and the better ones are selected by the selection operator. The pair paths selected by the selection operator are combined by the single-point crossover operator. After applying the crossover operator on the population, the mutation occurs on some of the new paths. When mutation occurs, some bits of the paths are randomly selected and their contents are changed randomly. After the operators are applied on the paths, the new paths need to be evaluated and the cost of each one to be calculated. Then, the previous steps must be repeated until the stop condition is met. The explained algorithm is represented in Fig. 5.

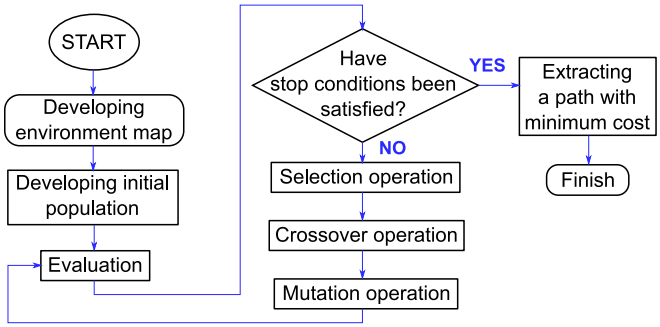

Fig. 5. The flow chart of the algorithm used for path planning.

III. Results

In this section, the results of curvature control of waterjet with changing depth-of-cut, along with a comparison to the modeling, and the results of path planning are presented.

TABLE I

Soft tissue phantoms, their properties, and corresponding waterjet velocities and depths-of-cut.

Tissue 1 (G1650 10%) $\alpha = 1.2472$			
Q($\frac{ml}{min}$)	v($\frac{m}{s}$)	$\mu(MPa)$	h (mm)
20	7.37	2.954	2.49
40	14.74	6.27	3.75

Tissue 2 (G1650 15%) $\alpha = 1.7008$				
Q($\frac{ml}{min}$)	v($\frac{m}{s}$)	$\mu(MPa)$	h (mm)	Fracture Toughness ($\frac{kJ}{m^2}$)
30	11.05	5.82	1.31	85.58
50	18.43	10.02	2.16	114.11

A. Curvature of the waterjet needle is a function of depth-of-cut of waterjet

In this section, it is shown that the waterjet curvature is a function of depth-of-cut of waterjet in soft tissue which in turn is dependent on tissue, and waterjet properties. Table I shows the soft tissue phantoms used, their properties from mechanical tests (at associated waterjet velocities), waterjet velocities, and the associated depths-of-cut. μ (MPa), and α are shear modulus, and strain hardening factor of soft tissue phantoms that are derived by fitting first-order Ogden model [26] to experimental stress-strain data of the tissues. The duration of time used for the depth-of-cut measurements and predictions is 30 seconds. The depth of cut is experimentally measured and also predicted from the mechanics-based model shown in 2. Tissue properties are measured from Split-Hopkinson-Pressure-Bar tests to be relevant to waterjet velocities (note that soft tissue goes through strain hardening at higher velocities).

Fig. 6, and Fig. 7 show the results of the waterjet needle steering in the z-y plane and the corresponding model of steering in two soft tissue simulants. As can be seen from the figures, the needle curvature can be controlled by changing the velocity of waterjet and thus depth-of-cut, and that the radius of curvature is smaller in the harder soft tissue simulant. The needle base has no rotation in either of these figures.

Fig. 8 shows an example of waterjet needle steering with a base rotation midway through the insertion. In this example, $\delta\ell$ = 2.2 mm with 10 steps for the first bend, $\delta\theta$ = 0 180°, and then 20 steps for the second bend of the insertion. $Q = 50\frac{ml}{min}$ is selected for both bends (to give cut-depth of $2.2mm$). An overlay of the model with the experimental results shows that the model can precisely predict the experiments.

B. Path planning results

In this section, several 2D needle paths are made to show the effectiveness of the proposed path planning method. For the first path, $\delta\theta$ is always zero (no rotation at the base). $\begin{bmatrix} 0 & 5 & 0 \end{bmatrix}^T$ mm , and $\begin{bmatrix} 0 & 30 & 40 \end{bmatrix}^T$ mm are beginning, and target points, respectively. The path has been constructed by 20 optimized steps. Fig. 9 shows this path with a high degree of overlap between the simulated and experimental results.

In the second example path, $\delta\theta$ is always zero except one 180° rotation. Beginning and target points are $\begin{bmatrix} 0 & 20 & 0 \end{bmatrix}^T$

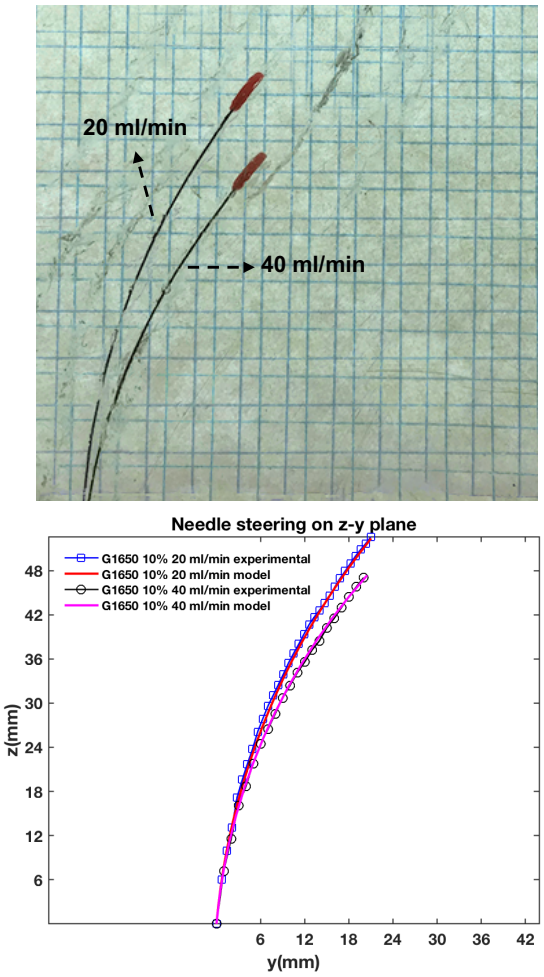

Fig. 6. An example of waterjet needle steering in the z-y plane in SEBS G1650 10% tissue simulant. (up) Experimental results of needle steering using two different waterjet velocities (two figures are overlaid on top of each other). (bottom) Experimental results (derived with image processing on successive photos of needle path to determine the tip position) along with the kinematic model. Average radii of curvature for three experiments are: For $20\frac{ml}{min}$: $r_{ave} = 97.25mm$ (total insertion length $\ell = 65$ mm), and for $40\frac{ml}{min}$: $r_{ave} = 81.79mm$ (total insertion length $\ell = 57$ mm).

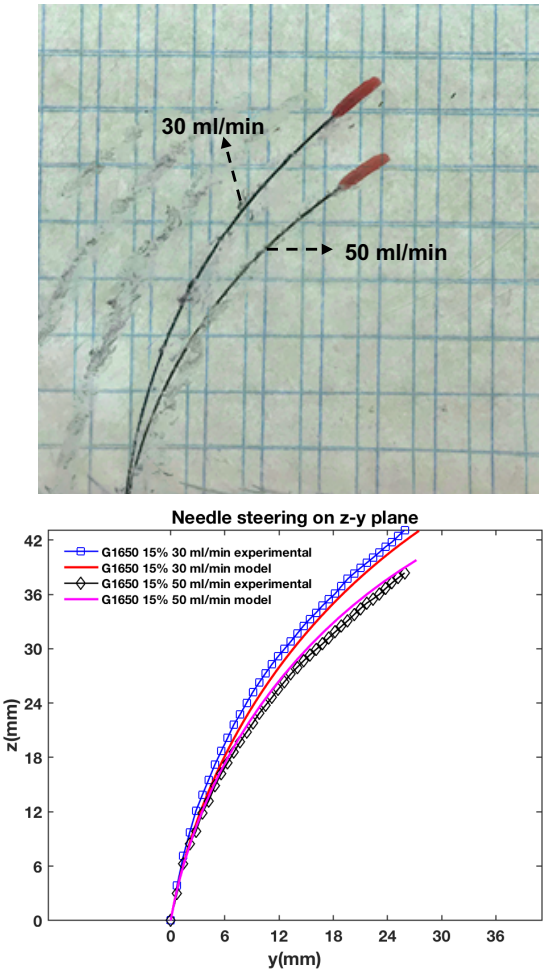

Fig. 7. An example of waterjet needle steering on z-y plane in SEBS G1650 15% tissue simulant. (up) Experimental results of needle steering using two different waterjet velocities (the figures are overlaid on top of each other). (bottom) Experimental results along with the kinematic model. Average radii of curvature for three experiments are: For $30\frac{ml}{min}$: $r_{ave} = 66.49mm$ (total insertion length $\ell = 56$ mm), and for $50\frac{ml}{min}$: $r_{ave} = 58.42mm$ (total insertion length $\ell = 52$ mm).

mm , and $\begin{bmatrix}0 & 20 & 44\end{bmatrix}^T$ mm, respectively. 20 optimized steps are used. Fig. 10 shows this path, again with agreement between the simulated trajectory and the experimental results.

In the third example, there is not any limitation on the rotation at the base of the needle, θ. The initial point and the target point are chosen differently for three different needle paths. The paths have been constructed by 40 optimized steps. The initial points and the target points are: $\begin{bmatrix}0 & 20 & 0\end{bmatrix}^T$ mm , and $\begin{bmatrix}0 & 90 & 90\end{bmatrix}^T$ mm, $\begin{bmatrix}0 & 20 & 0\end{bmatrix}^T$ mm , and $\begin{bmatrix}0 & 90 & 20\end{bmatrix}^T$ mm, and $\begin{bmatrix}0 & 90 & 0\end{bmatrix}^T$ mm , and $\begin{bmatrix}0 & 5 & 90\end{bmatrix}^T$ mm, respectively.

Fig. 11 shows the optimized paths. As can be seen from the figure, the direction of the needle curvature can be controlled by varying waterjet velocity and controlling the depth-of-cut by changing the volumetric flow rate of the pump. It is also evident from this figure that the needle can reach multiple targets by one insertion into the tissue.

IV. DISCUSSION

In this paper, a new class of steerable needles that we call fracture-directed waterjet steerable needles is presented in which the direction of the tissue fracture is controlled by sub-millimeter waterjet that is subsequently followed by the flexible Nititnol needle. This paper characterizes the developed waterjet steerable needle using two different tissue stiffnesses and 4 different waterjet velocities. The results show that by varying the velocity of the waterjet and thus cut-depth of the waterjet in soft tissue, the curvature can be controlled. This promises a better method for curvature control in comparison to the steerable needle literature where duty cycling (continual spinning of the needle) is used to control curvature [8], [27], [28], [29]. Duty-cycle methods must account for the inherent torsional windup associated with twisting a long, super-elastic needle about the insertion axis[30], [31]. Thus, waterjet steerable needles promise a

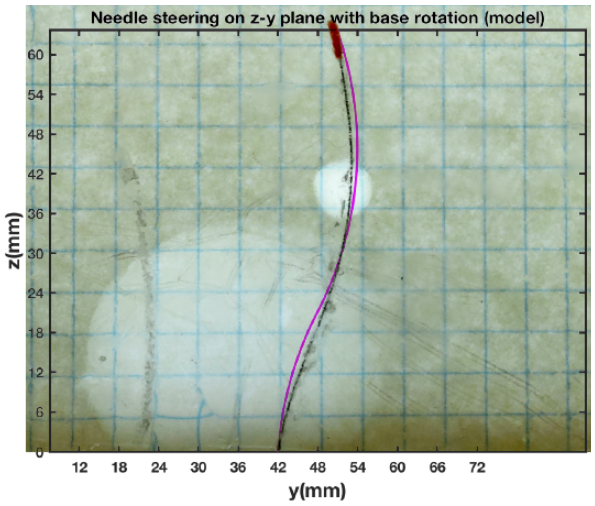

Fig. 8. An example of waterjet needle steering with a base rotation during the insertion. In this example, $\delta\ell$ = 2.2 2.2 mm with 10 steps for the first bend, $\delta\theta$ = 0 180° to flip the nozzle direction, and 20 steps for the second bend. $Q = 50 \frac{ml}{min}$ for both bends. The figure shows an overlap of the experimental result with the model.

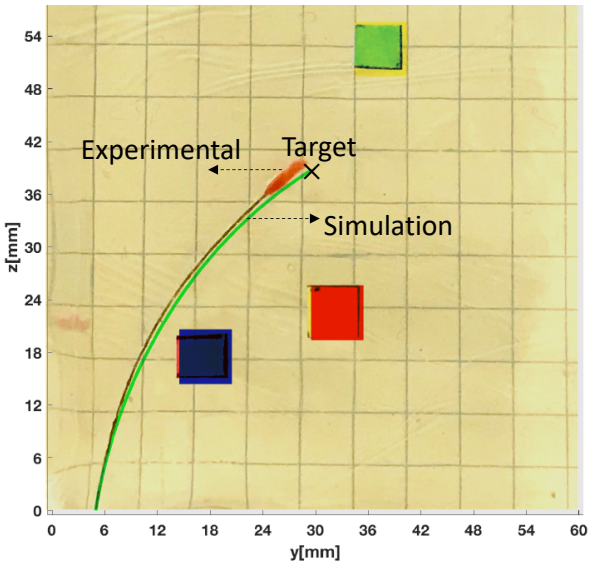

Fig. 9. 2D path planning of the waterjet steerable needle with no base rotation. The Figure shows an overlap of the simulated path and experimental results.

better control over the tissue fracture and needle curvature that was unattainable with traditional steerable needles.

V. CONCLUSIONS AND FUTURE WORK

In this paper, a new class of steerable needles, namely waterjet steerable needles (in which the direction of the tissue fracture is controlled by waterjet and then the flexible needle follows) is presented. The radii of curvature of needle for two tissue stiffnesses and 4 different waterjet velocities are investigated. The results showed that the curvature of the needle can be controlled by varying waterjet velocity and thus controlling the depth of cut. A mechanics-based model for depth-of-cut as the main input to the system is presented

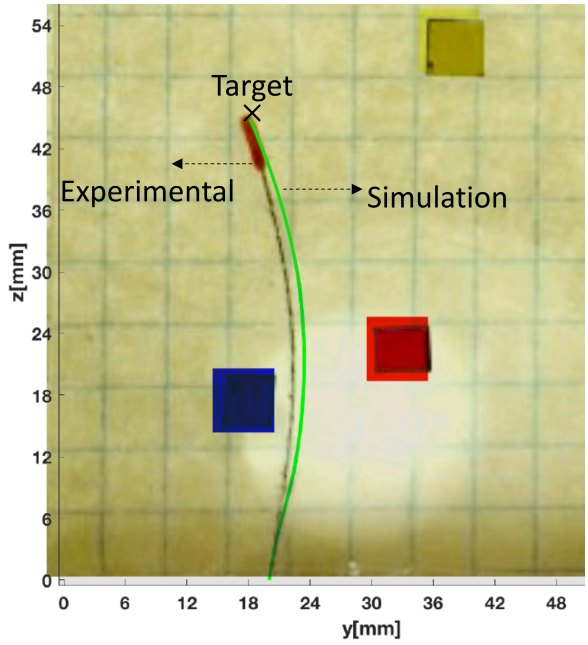

Fig. 10. 2D path planning of the waterjet steerable needle with one 180° base rotation. The Figure shows an overlap of the simulated path and experimental result.

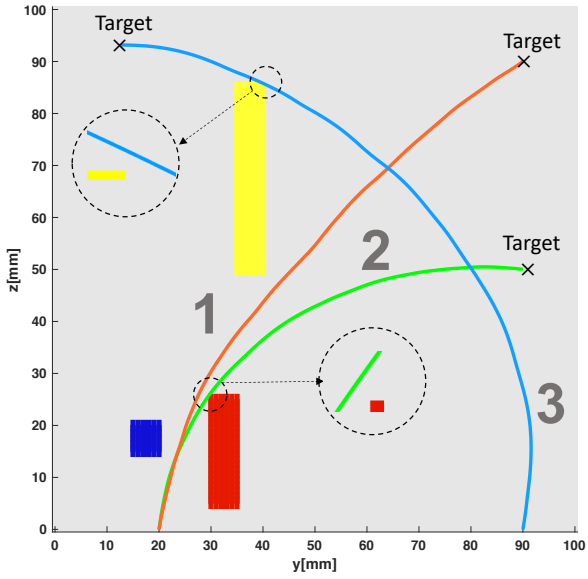

Fig. 11. 2D path planning of the waterjet steerable needle with different base rotations. As can be seen from this figure, the curvature of the waterjet steerable needle can be controlled by changing the depths-of-cut of waterjet that can be controlled by changing the velocity of waterjet. It can also be seen from this figure that the waterjet steerable needle can reach different targets from one insertion in the soft tissue.

and a unicycle model with the depth of cut as the main parameter defines a model of the kinematic motion of the needle. A genetic algorithm used to achieve path planning in 2D is also presented.

Curvature of the needle is also dependent on the waterjet tip angle, and in this paper a constant angle 30° nozzle is used. Future research involves developing controllable nozzles to further control the curvature as depicted in Fig. 1. The current limitation of the system is developing sub-millimeter waterjet tips with accurate angle with current machining techniques on the current materials. Future research also involves extending the current study to animal studies to see how the needle performs in real living tissues.

ACKNOWLEDGMENT

The authors would like to thank Alex Rodrigues and Sean Journot for their help in the experimental setup as well as Kraton Polymers LLC to provide samples of Kraton G1650 for research.

REFERENCES

[1] P. J. Swaney, A. W. Mahoney, B. I. Hartley, A. A. Remirez, E. Lamers, R. H. Feins, R. Alterovitz, and R. J. Webster III, "Toward transoral peripheral lung access: Combining continuum robots and steerable needles," *Journal of medical robotics research*, vol. 2, no. 01, p. 1750001, 2017.

[2] M. Abayazid, P. Moreira, N. Shahriari, A. Zompas, and S. Misra, "Three-dimensional needle steering using automated breast volume scanner (abvs)," *Journal of medical robotics research*, vol. 1, no. 01, p. 1640005, 2016.

[3] P. Moreira, G. van de Steeg, T. Krabben, J. Zandman, E. E. Hekman, F. van der Heijden, R. Borra, and S. Misra, "The miriam robot: A novel robotic system for mr-guided needle insertion in the prostate," *Journal of medical robotics research*, vol. 2, no. 04, p. 1750006, 2017.

[4] T. Lehmann, R. Sloboda, N. Usmani, and M. Tavakoli, "Model-based needle steering in soft tissue via lateral needle actuation," *IEEE Robotics and Automation Letters*, vol. 3, no. 4, pp. 3930–3936, 2018.

[5] N. J. Cowan, K. Goldberg, G. S. Chirikjian, G. Fichtinger, R. Alterovitz, K. B. Reed, V. Kallem, W. Park, S. Misra, and A. M. Okamura, "Robotic needle steering: Design, modeling, planning, and image guidance," in *Surgical robotics*. Springer, 2011, pp. 557–582.

[6] M. Scali, T. P. Pusch, P. Breedveld, and D. Dodou, "Needle-like instruments for steering through solid organs: A review of the scientific and patent literature," *Proceedings of the Institution of Mechanical Engineers, Part H: Journal of Engineering in Medicine*, vol. 231, no. 3, pp. 250–265, 2017.

[7] S. Misra, K. B. Reed, A. S. Douglas, K. Ramesh, and A. M. Okamura, "Needle-tissue interaction forces for bevel-tip steerable needles," in *2008 2nd IEEE RAS & EMBS International Conference on Biomedical Robotics and Biomechatronics*. IEEE, 2008, pp. 224–231.

[8] P. J. Swaney, J. Burgner, H. B. Gilbert, and R. J. Webster, "A flexure-based steerable needle: high curvature with reduced tissue damage," *IEEE Transactions on Biomedical Engineering*, vol. 60, no. 4, pp. 906–909, 2012.

[9] T. K. Adebar, J. D. Greer, P. F. Laeseke, G. L. Hwang, and A. M. Okamura, "Methods for improving the curvature of steerable needles in biological tissue," *IEEE Transactions on Biomedical Engineering*, vol. 63, no. 6, pp. 1167–1177, 2015.

[10] C. Rossa and M. Tavakoli, "Issues in closed-loop needle steering," *Control Engineering Practice*, vol. 62, pp. 55–69, 2017.

[11] A. Yamada, S. Naka, N. Nitta, S. Morikawa, and T. Tani, "A loop-shaped flexible mechanism for robotic needle steering," *IEEE Robotics and Automation Letters*, vol. 3, no. 2, pp. 648–655, 2017.

[12] M. Khadem, C. Rossa, N. Usmani, R. S. Sloboda, and M. Tavakoli, "Robotic-assisted needle steering around anatomical obstacles using notched steerable needles," *IEEE journal of biomedical and health informatics*, vol. 22, no. 6, pp. 1917–1928, 2017.

[13] S. L. Charreyron, E. Gabbi, Q. Boehler, M. Becker, and B. J. Nelson, "A magnetically steered endolaser probe for automated panretinal photocoagulation," *IEEE Robotics and Automation Letters*, vol. 4, no. 2, pp. xvii–xxiii, 2018.

[14] J. H. Rogers, B. R. Stripe, G. D. Singh, W. D. Boyd, D. Fan, and T. W. Smith, "Initial clinical experience with the flexpoint steerable transseptal needle in left-sided structural heart procedures," *Catheterization and Cardiovascular Interventions*, vol. 92, no. 4, pp. 792–796, 2018.

[15] Z. Wang, I. Reed, and A. M. Fey, "Toward intuitive teleoperation in surgery: Human-centric evaluation of teleoperation algorithms for robotic needle steering," in *2018 IEEE International Conference on Robotics and Automation (ICRA)*. IEEE, 2018, pp. 1–8.

[16] T. Lehmann, R. Sloboda, N. Usmani, and M. Tavakoli, "Human–machine collaboration modalities for semi-automated needle insertion into soft tissue," *IEEE Robotics and Automation Letters*, vol. 3, no. 1, pp. 477–483, 2017.

[17] T. Greigarn, N. L. Poirot, X. Xu, and M. C. Çavuşoğlu, "Jacobian-based task-space motion planning for mri-actuated continuum robots," *IEEE robotics and automation letters*, vol. 4, no. 1, pp. 145–152, 2018.

[18] J. P. Swensen, M. Lin, A. M. Okamura, and N. J. Cowan, "Torsional dynamics of steerable needles: modeling and fluoroscopic guidance," *IEEE Transactions on Biomedical Engineering*, vol. 61, no. 11, pp. 2707–2717, 2014.

[19] F. Yang, M. Babaiasl, and J. P. Swensen, "Fracture-directed steerable needles," *Journal of Medical Robotics Research*, vol. 4, no. 01, p. 1842002, 2019.

[20] M. Babaiasl, F. Yang, and J. P. Swensen, "Towards water-jet steerable needles," in *2018 7th IEEE International Conference on Biomedical Robotics and Biomechatronics (Biorob)*. IEEE, 2018, pp. 601–608.

[21] M. Babaiasl, F. Yang, Y. Chen, J.-L. Ding, and J. P. Swensen, "Predicting depth of cut of water-jet in soft tissue simulants based on finite element analysis with the application to fracture-directed water-jet steerable needles," in *2019 International Symposium on Medical Robotics (ISMR)*. IEEE, 2019, pp. 1–7.

[22] R. A. Mrozek, B. Leighliter, C. S. Gold, I. R. Beringer, H. Y. Jian, M. R. VanLandingham, P. Moy, M. H. Foster, and J. L. Lenhart, "The relationship between mechanical properties and ballistic penetration depth in a viscoelastic gel," *Journal of the mechanical behavior of biomedical materials*, vol. 44, pp. 109–120, 2015.

[23] N. Abolhassani, R. Patel, and M. Moallem, "Control of soft tissue deformation during robotic needle insertion," *Minimally invasive therapy & allied technologies*, vol. 15, no. 3, pp. 165–176, 2006.

[24] R. J. Webster III, J. S. Kim, N. J. Cowan, G. S. Chirikjian, and A. M. Okamura, "Nonholonomic modeling of needle steering," *The International Journal of Robotics Research*, vol. 25, no. 5-6, pp. 509–525, 2006.

[25] T. K. Adebar and A. M. Okamura, "Recursive estimation of needle pose for control of 3d-ultrasound-guided robotic needle steering," in *2014 IEEE/RSJ International Conference on Intelligent Robots and Systems*. IEEE, 2014, pp. 4303–4308.

[26] R. Ogden, G. Saccomandi, and I. Sgura, "Fitting hyperelastic models to experimental data," *Computational Mechanics*, vol. 34, no. 6, pp. 484–502, 2004.

[27] M. Fu, A. Kuntz, R. J. Webster, and R. Alterovitz, "Safe motion planning for steerable needles using cost maps automatically extracted from pulmonary images," in *2018 IEEE/RSJ International Conference on Intelligent Robots and Systems (IROS)*. IEEE, 2018, pp. 4942–4949.

[28] D. S. Minhas, J. A. Engh, M. M. Fenske, and C. N. Riviere, "Modeling of needle steering via duty-cycled spinning," in *2007 29th Annual International Conference of the IEEE Engineering in Medicine and Biology Society*. IEEE, 2007, pp. 2756–2759.

[29] A. Majewicz, J. J. Siegel, A. A. Stanley, and A. M. Okamura, "Design and evaluation of duty-cycling steering algorithms for robotically-driven steerable needles," in *2014 IEEE International Conference on Robotics and Automation (ICRA)*. IEEE, 2014, pp. 5883–5888.

[30] K. B. Reed, A. M. Okamura, and N. J. Cowan, "Modeling and control of needles with torsional friction," *IEEE Trans. Biomed. Eng.*, vol. 56, no. 12, pp. 2905–2916, Dec. 2009, nIHMS192959. [Online]. Available: http://dx.doi.org/10.1109/TBME.2009.2029240

[31] J. P. Swensen and N. J. Cowan, "Torsional dynamics compensation enhances robotic control of tip-steerable needles," in *Robotics and Automation (ICRA), 2012 IEEE International Conference on*. IEEE, 2012, pp. 1601–1606.